



ELSEVIER

## Time-of-propagation Cherenkov counter for particle identification

M. Akatsu<sup>a</sup>, M. Aoki<sup>a</sup>, K. Fujimoto<sup>a</sup>, Y. Higashino<sup>a</sup>, M. Hirose<sup>a</sup>, K. Inami<sup>a</sup>,  
A. Ishikawa<sup>a</sup>, T. Matsumoto<sup>a</sup>, K. Misono<sup>a</sup>, I. Nagai<sup>a</sup>, T. Ohshima<sup>a</sup>, A. Sugi<sup>a</sup>,  
A. Sugiyama<sup>a</sup>, S. Suzuki<sup>a,\*</sup>, M. Tomoto<sup>a</sup>, H. Okuno<sup>b</sup>

<sup>a</sup>Physics Department, Nagoya University, Chikusa-ku, Furo-cho, Nagoya 464-8602, Japan

<sup>b</sup>IPNS, High Energy Accelerator Research Organization (KEK), Ibaraki 305-0801, Japan

Received 24 March 1999; received in revised form 5 July 1999; accepted 6 July 1999

### Abstract

We describe here a new concept of a Cherenkov detector for particle identification by means of measuring the Time-of-Propagation (TOP) of Cherenkov photons. © 2000 Elsevier Science B.V. All rights reserved.

### 1. Introduction

Particle-identification (PID) capability plays an essential role in experiments at B-factories. Especially,  $\pi/K$  identification in the momentum range up to  $4\text{ GeV}/c$  over a wide angular region is crucially important for the primary physics goals to measure CP violation. In the Belle detector at KEK-B, a combination of Aerogel Cherenkov counters, TOF counters and  $dE/dX$  measurement in a central drift chamber (CDC) provides PID information for charged particles.<sup>1</sup> Although the present detector system covers most of the momentum region of the charged particles, the PID power for a particle with momentum above

$3\text{ GeV}/c$  is not sufficiently satisfactory. Concerning the future upgrade of PID devices, we discuss here the effectiveness of measuring both the Time-of-Propagation (TOP) and the emission angle of the Cherenkov photons.

The time resolution of the Time-of-Flight (TOF) counter using a plastic scintillator is inherently limited by the following effects besides the transit-time spread (TTS) of a phototube: (1) a finite decay time of photon emission, and (2) a different photon propagation length or propagation time in the scintillator to a phototube, depending on the photon emission angle. Thus, the conventional TOF counter measures the arrival time of the earliest photons out of many, whereby the remaining large amount of photons are not effectively used for the time measurement. While effect (1) cannot be reduced as far as the scintillation is concerned, effect (2) can be resolved by measuring the arrival times of the earliest photons as a function of the photon emission angle, since, in the total-reflection-type scintillator bar, most photons propagate in the

\*Corresponding author. Tel.: +81-52-789-2893; fax: +81-52-782-5752.

E-mail address: [suzuki@hepl.phys.nagoya-u.ac.jp](mailto:suzuki@hepl.phys.nagoya-u.ac.jp) (S. Suzuki)

<sup>1</sup> For the description of the KEKB factory and the BELLE detector, for instance, see Refs. [1,2].

scintillator while keeping their original emission angles. This two-dimensional information could improve the time original emission angles. This two-dimensional information could improve the time resolution, depending on the number of angular segmentations of the photon detector and on the number of photons collected at each segment.

When Cherenkov radiation is utilized, although its number of produced photons is much smaller than in the scintillation case, effect (1) can, in principle, be disregarded. In addition, since the Cherenkov photon emission angle is uniquely determined by the particle velocity ( $\beta$ ) and since the propagation time of photons in a light guide of an internal-total-reflection type can be calculated as a function of the photon emission angle, a measurement of a correlation between TOP and the photon emission angle could provide PID information by itself, as we propose below.

In the DIRC concept [3–8], Cherenkov photons produced by a quartz radiator are transported to

an end of the radiator by means of internal total reflection, and its ring image is magnified and projected onto a photon-detector plane placed at the bar end. A basic study of this concept clearly proved that a photon is effectively transported in the long quartz bar, preserving its original photon direction. The Babar detector at SLAC adopted this concept for PID, and introduced a large stand-off photon detection system in order to ineffectuate the finite size of the quartz cross section onto the ring image [6–8]. On the other hand, Kamae et al. [9–11] proposed a compact focussing type of DIRC using a small mirror instead of a large stand-off system. This approach suits particles incident normal to the quartz bar, but for inclined particles the ring image is distorted due to the finite quartz cross section. To make this image-fusing effect insignificant, the size and geometry of the focussing mirror become unfeasible [12].

We propose here a new concept for the Cherenkov-ring image detector, the TOP detector. The two-dimensional information of the ring image is

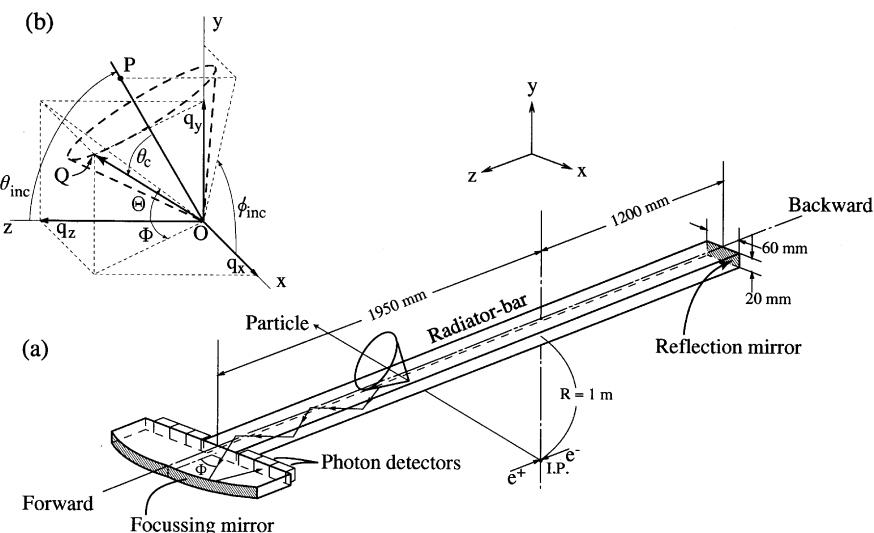


Fig. 1. (a) Schematic structure of the TOP detector. The detector comprises a quartz radiator-bar (20 mm-thick, 60 mm-wide, 3150 mm-long) and two mirrors for focussing (the butterfly-shaped one at the forward end) and reflecting (the flat one at the backward end). The Cherenkov photons are horizontally focussed onto the photon-detector plane, and their time and angle information ( $t_p + t_f$  and  $\Phi$ ) are measured by position-sensitive multi-channel phototubes. (b) The relation among the basic variables in the  $(x, y, z)$  coordinate system.  $\theta_c$  is the Cherenkov angle. OP indicates the particle trajectory, the direction of which is defined by  $\theta_{inc}$  and  $\phi_{inc}$ . OQ is the unit velocity vector of a Cherenkov photon, of which the direction is defined by  $\Phi$  and  $\Theta$  and its directional components are denoted as  $q_x$ ,  $q_y$ , and  $q_z$ .

represented by the TOP of the Cherenkov photon and its horizontal angle ( $\Phi$ ; see Fig. 1). The use of TOP information with an appropriate focussing mirror makes the image-fusing effect be disregarded and compactification can be realized while maintaining the high enough PID ability. We describe below the basic concept, characteristic features, practical configurations and simulation results on the TOP detector, and discuss some issues for making it a realistic device.

We should mention a paper by Honsheid et al. [13], which we noted after our detailed analysis had been completed. It discusses the Cherenkov Correlated Timing (CCT) detector: CCT [13–15] is a kind of TOF counter with a single phototube readout for detecting early arriving photons of Cherenkov radiation. In Ref. [6] a similar concept as ours can be found, although no detailed study is presented and the focussing mirror approach is not introduced.

## 2. Conceptual design and expected properties

The principal structure of the TOP counter in the  $(x, y, z)$  coordinate system is illustrated in Fig. 1. When a charged particle passes through the radiator bar, Cherenkov photons are emitted in a conical direction defined by the emission angle ( $\theta_C$ ), where  $\cos \theta_C = 1/n\beta$ ,  $n$  = refractive index. Then, photons propagate to both or either ends by means of total reflection on the internal bar surface. Photons propagating backward are reflected by a flat mirror at the end. At the forward end, photons are horizontally focused by a butterfly-shaped mirror onto a plane where position-sensitive multi-anode phototubes are equipped to measure TOP as a function of the  $\Phi$ -angle.

### 2.1. $t_p$ and $\Phi$

The TOP is determined only by the  $z$ -component of the light velocity in the quartz bar as

$$\begin{aligned} t_p &= \left( \frac{L}{c/n(\lambda)} \right) \times \left( \frac{1}{q_z} \right) \\ &= 4.90 \text{ (ns)} \times \frac{L \text{ (m)}}{q_z} \end{aligned} \quad (1)$$

where  $t_p$  is the photon propagation time (TOP),  $L$  is the overall distance from the photon emission point to the detector,  $n(\lambda)$  is the refractive index of the quartz at wavelength  $\lambda$ ,  $c$  is the light velocity in a vacuum, and  $q_z$  is the directional  $z$ -component of the photon emission.

Denoting the polar and azimuthal angles of an incident charged particle as  $\theta_{\text{inc}}$  and  $\phi_{\text{inc}}$  (see Fig. 1), respectively, the directional components of the photon velocity  $q_i$  ( $i = x, y, z$ ) are written as

$$\begin{aligned} q_x &= q_{x'} \cos \theta_{\text{inc}} \cos \phi_{\text{inc}} - q_{y'} \sin \phi_{\text{inc}} \\ &\quad + q_{z'} \sin \theta_{\text{inc}} \cos \phi_{\text{inc}} \\ q_y &= q_{x'} \cos \theta_{\text{inc}} \sin \phi_{\text{inc}} + q_{y'} \cos \phi_{\text{inc}} \\ &\quad + q_{z'} \sin \theta_{\text{inc}} \sin \phi_{\text{inc}} \\ q_z &= -q_{x'} \sin \theta_{\text{inc}} + q_{z'} \cos \theta_{\text{inc}} \end{aligned} \quad (2)$$

where  $q_i$ 's ( $i = x', y', z'$ ) are the directional components of the photon emission in the frame where the particle moves along the  $z'$ -axis:

$$\begin{aligned} q_{x'} &= \sin \theta_C \cos \phi_C \\ q_{y'} &= \sin \theta_C \sin \phi_C \\ q_{z'} &= \cos \theta_C. \end{aligned} \quad (3)$$

The horizontal and vertical photon angles at the bar end are then given as

$$\begin{aligned} \Phi &= \arctan \left( \frac{q_x}{q_z} \right) \\ \Theta &= \arctan \left( \frac{q_y}{q_z} \right). \end{aligned} \quad (4)$$

The  $\phi_C$  angle of Cherenkov photons distributes uniformly over  $2\pi$ . When we fix  $\phi_C$ , individual three-directional components ( $q_i$ ) are uniquely related to  $\theta_C$ . Therefore, a measurement of any two directional components or any two combinations of them among Eqs. (3) and (4) provides information about  $\theta_C$ .

Accordingly, in a TOP concept, we use the two parameters ( $q_z, \Phi$ ) for extracting  $\theta_C$ , while in DIRC, ( $\Theta, \Phi$ ) are used. The advantage of our approach is that the  $q_z$  measurement is not seriously influenced by the quartz bar cross section.

## 2.2. Accuracy of the TOP measurement

Here, we estimate various contributions to the accuracy of the TOP measurement with a detector which we are preparing for R&D work. By modelling the detector are presented in Fig. 1, the parameters of each element and the expected machining or construction accuracy are assumed as described below.

The size of the radiator bar is 20 mm-thick (in  $y$ ), 60 mm-wide (in  $x$ ), and about 3 150 mm (in  $z$ ), on which a butterfly-shaped focussing mirror block and a flat reflection mirror are attached at the forward and backward ends, respectively. The focussing mirror comprises two sub-elements, each forming an arc of a circle with a radius of 250 mm. As a PID detector for the Belle experiment, we suppose these detectors to be placed at  $R = 1$  m from the beam axis to form a cylindrical configuration, and due to an asymmetric-energy collider the detector is asymmetrically configured with respect to the  $z$ -direction to cover the polar angle from  $30^\circ$  to  $140^\circ$  in the lab-frame. For simplicity of calculation, the photon-propagation length in the focussing mirror is set as 20 cm for all photons.

The material of the radiator bar and the mirrors is synthetic optical quartz (SUPRASIL-P30) manufactured by Shin-etsu Quartz Co. and their surfaces are polished by Baikowski-Japan Co. with a flatness of  $\pm 5 \mu\text{m}$ . The quartz has a refractive index of  $n = 1.47$  at a wavelength ( $\lambda$ ) of 390 nm and a transmittance of 90%/m at  $\lambda = 250$  nm. The reflecting surface of the mirrors comprises aluminium of a few 100 nm-thick on 200 Å-thick chromium by evaporation, which provides a reflection efficiency of 98%. The photon detector (R5900U-00-L16) is a multi-anode (16 channel) linear array phototube with a bialkali window by Hamamatsu Photonics Co. Although this tube does not function under a magnetic field, it has a quite suitable TTS for our early R&D work without a magnetic field.

Now, by taking the above structure of the TOP counter into account, we estimate various contributions to the accuracy of the PID measurement.

(1)  $\lambda$ -dependence of  $n$ : The refractive index ( $n(\lambda)$ ) of the quartz varies depending on  $\lambda$ . As a result, the Cherenkov angle ( $\theta_C$ ) and the total reflection angle vary for individual photons in addition to the

propagation velocity. The effect to TOP is

$$\frac{\sigma_{t_p}}{t_p} = \left( \frac{\sigma_n}{n} \right) \times (1 - \alpha) \quad (5)$$

where

$$\alpha = n \left( \frac{\partial q_z / \partial n}{q_z} \right). \quad (6)$$

Accounting for the  $\lambda$ -dependence of the Cherenkov photon yield and the  $\lambda$ -dependent quantum efficiency of the phototube, we take  $n = 1.47 \pm 0.008$  ( $\Delta n/n = 5 \times 10^{-3}$ ) for the numerical calculation described in the next sub-section.

(2) *Angular resolution*: The  $\Phi$ -angle resolution depends on the position resolution of the phototube and the focussing accuracy of the mirror. The designed focussing mirror has a resolution of  $\sigma = 0.8$  mm with a dispersion of  $d\Phi/dx = 0.5^\circ/\text{mm}$ . Since the phototube has a 0.8 mm anode width, as described below, the  $\Phi$  resolution is evaluated as  $\sigma_\phi \approx 0.5^\circ$ .

The  $\Phi$ -dependent behaviour of this effect on  $t_p$  shows a steep increase with  $\Phi$ , but a very small contribution at small  $\Phi$ -angles, as numerically discussed in the next subsection. This limits the  $\Phi$  aperture to be  $|\Phi| \leq 45^\circ$ .

(3) *TTS of the phototube*: The phototube (R5900U-00-L16) has a 16 mm  $\times$  16 mm photo-sensitive area, which is segmented into 16 strips with an area of 0.8 mm  $\times$  16 mm and a 0.2 mm space between adjacent strips. The quantum efficiency (QE) is 25% at 400 nm and  $\sigma_{\text{TTS}} \approx 70$  ps with a pulse rise-time of 0.6 ns for a single photoelectron.

(4) *Timing accuracy of the start signal*: We expect a start timing accuracy of 25 ps from the RF signal of the accelerator.

(5) *Effect of the quartz thickness*: Because relativistic particle takes 66 ps to pass through the 20 mm-thick quartz, the time spread of the Cherenkov photon emission is estimated to be  $\sigma_{\text{thick}} = 20$  ps ( $= 66/\sqrt{12}$ ). When the incident particle is inclined with respect to the normal of the bar surface, the time-spread becomes much smaller due to cancellation of the particle flight-time and the photon propagation-time. For instance,  $\sigma_{\text{thick}}$  is 6 ps and 10 ps at  $\theta_{\text{inc}} = 30^\circ$  and  $60^\circ$ , respectively.

(6) *Effect of the charged-particle tracking accuracy:* In the Belle detector, the  $z$  position of a charged-particle track is measured by the central drift chamber (CDC) with an accuracy of about 2 mm. This means that it corresponds to a time uncertainty of 10 ps.

On the other hand, the accuracy of the momentum measurement is related to the accuracy of the Cherenkov angle as

$$\sigma_{\theta_c} = \left( \frac{\cot \theta_c}{\gamma^2} \right) \times \left( \frac{\sigma_p}{p} \right). \quad (7)$$

Since the Cherenkov angle satisfies  $\cot \theta_c \sim 1$  for our particles and the CDC provides  $\sigma_p/p \approx 5 \times 10^{-3}$ ,  $\sigma_{\theta_c}$  can be ignored compared with the difference in the Cherenkov angle between  $\pi$  and  $K$ . The former is on the order of  $10^{-2}$ – $10^{-3}$  smaller than the latter. For instance,  $\Delta(\theta_c(\pi) - \theta_c(K)) = 6.5$  mrad, while  $\sigma_{\theta_c}$  is  $7 \times 10^{-3}$  and  $7 \times 10^{-2}$  mrad for  $4 \text{ GeV}/c \pi$  and  $K$ , respectively.

The accuracy of the incident-angle measurement contributes to the accuracy of the TOP measurement as

$$\frac{\sigma_{t_p}}{t_p} = - \left( \frac{1}{q_z} \right) \times \left( \frac{\partial q_z}{\partial \theta_{\text{inc}}} \right) \sigma_{\theta_{\text{inc}}} \quad (8)$$

and

$$\frac{\sigma_{t_p}}{t_p} = - \left( \frac{1}{q_z} \right) \times \left( \frac{\partial q_z}{\partial \phi_{\text{inc}}} \right) \sigma_{\phi_{\text{inc}}} = 0. \quad (9)$$

The effect of any  $\theta_{\text{inc}}$  ambiguity on  $t_p$  is evaluated to be less than 10 ps in the case of the Belle detector.<sup>1</sup> It is an order-of-magnitude smaller than the contribution from item (3) ( $\sigma_{\text{TTS}} \approx 70$  ps), and is thus disregarded. Furthermore, it is, on the other hand, a specific feature of our approach that the  $t_p$  is independent of  $\phi_{\text{inc}}$ , as is obvious from Eq. (2). Therefore, the  $\phi_{\text{inc}}$  ambiguity does not intrinsically affect the TOP measurement.

### 2.3. Expected separability

From the above, the uncertainty of the TOP measurement arises predominantly from the effects of items (1)–(3). In order to understand the TOP behaviour and to evaluate the size of the above effects to TOP and the PID power, a calculation is performed with the following conditions. The  $\lambda$  dependence of the refractive index is disregarded, but its effect is represented by  $n = 1.47 \pm 0.008$  in Eq. (5); the  $\Phi$  resolution is set as  $\sigma_\phi = 0.5^\circ$ ; the effects of items (4) and (5) and the digitization bin of 25 ps are included into (3) to make an effective  $\sigma_{\text{TSS}} = 80$  ps (denoted hereafter as (3)'); the efficiencies of photon propagation and reflection are assumed to be 100%.

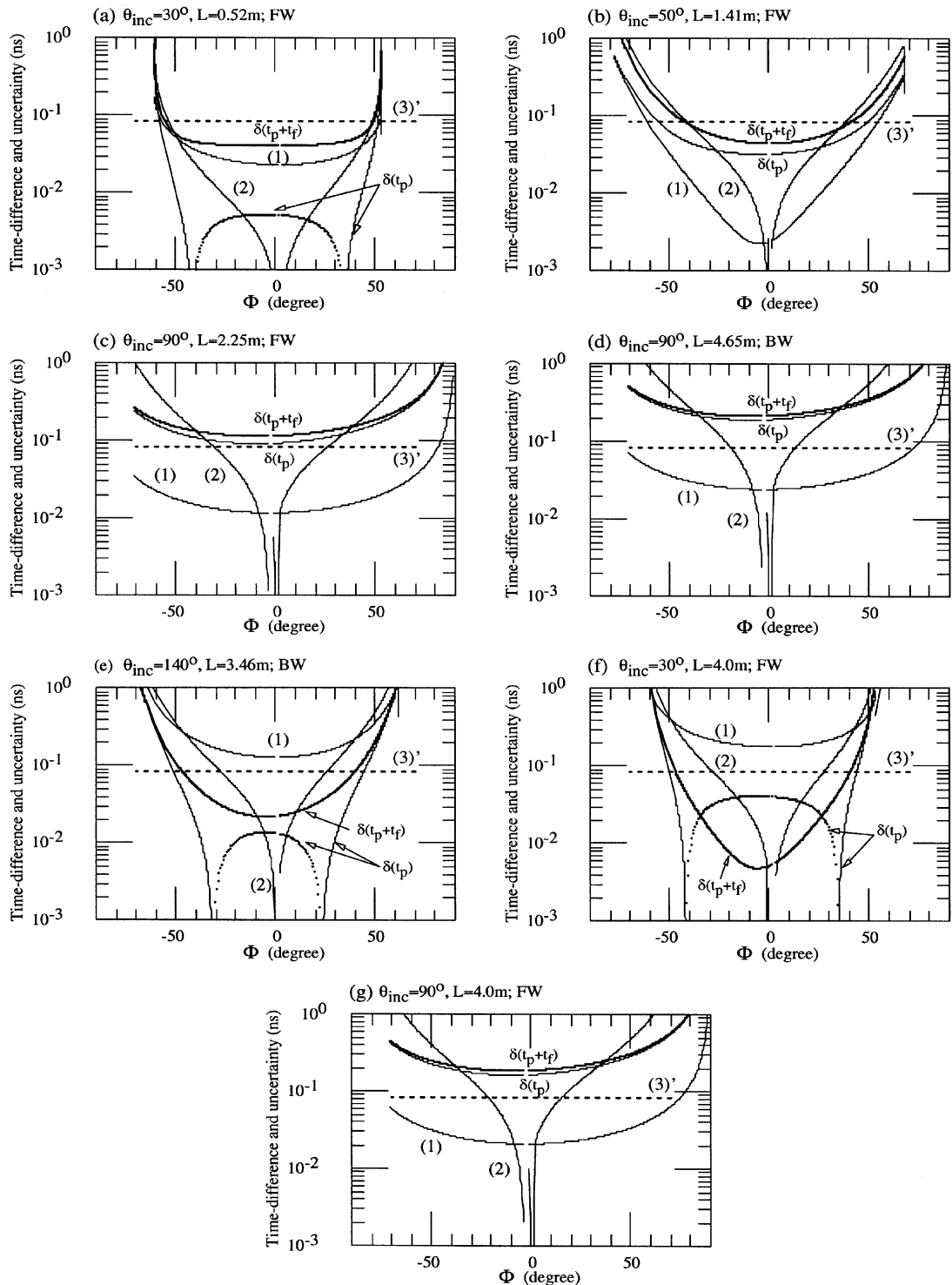
For PID in the collider geometry, in addition to the TOP measurement, we added to the  $t_p$  the particle's flight time  $t_f$  (TOF) from the colliding point to the quartz radiator placed at  $R = 1$  m: the measured time  $t = t_p + t_f$ .

#### 2.3.1. $\delta(t_p + t_f)$ and individual effects

In Fig. 2, the individual uncertainties of items (1), (2) and (3)' are shown for various cases of the incident angle ( $\theta_{\text{inc}}$ ), in addition to the  $t_p + t_f$  and  $t_p$  differences between  $4 \text{ GeV}/c \pi$  and  $K$  (denoted hereafter as  $\delta(t_p + t_f)$  and  $\delta(t_p)$ , respectively). (The propagation length ( $L$ ) in Figs. 2(a)–(e) is uniquely determined for each  $\theta_{\text{inc}}$  by assuming the particle coming from the colliding point under our geometry. On the other hand, the length ( $L$ ) in Figs. 2(f) and (g) is not real, but hypothetical, only for discussion purposes.) The asymmetries seen in the figures are caused by deflection of the azimuthal angle of the incident particle due to an axial magnetic field of 1.5 T.

At normal incidence (see, Figs. 2(c), (d) and (g)), effect (1) is an order of magnitude smaller than  $\delta(t_p)$ ; this relation holds irrespective of  $L$ , because of their

Fig. 2.  $t_p + t_f$  and  $t_p$  differences between  $\pi$  and  $K$ ,  $\delta(t_p + t_f)$  and  $\delta(t_p)$ , with a momentum of  $4 \text{ GeV}/c$  and expected time uncertainties from effects (1), (2) and (3)' for 7 different conditions. Individual conditions are indicated at the top of each figure. Especially, (a)–(e) correspond to the condition that the particle produced at the colliding point with  $\theta_{\text{inc}}$  flies  $R = 1$  m under a 1.5 T magnetic field and hit the TOP detector with the geometry illustrated in Fig. 1. The Cherenkov photons which propagate directly to the forward (FW)/backward (BW) ends are considered to be detected separately. The negative value of the  $\delta(t_p)$  is plotted by the dotted curves in (a), (e) and (f). Details are described in the text.



proportionality to  $L$ . Effect (2) has a strong  $\Phi$  dependence. In the region of the small  $\Phi$ -angle the effect is negligible, while in the large- $\Phi$  region it becomes dominant in determining the resolution. Mostly from this fact, the  $\Phi$ -angle aperture is limited to  $|\Phi| \leq 45^\circ$ , where the TOP measurement uncertainty is comparable to or less than  $\delta(t_p + t_f)$  under most of the incident-particle conditions. On the other hand, because  $\theta_{\text{inc}}$  deviates from normal incidence the value of  $\alpha$  decreases, and item (1) gives almost the same order of magnitude as  $\delta(t_p + t_f)$  at  $\theta_{\text{inc}} = 30^\circ$  (Fig. 2(a)), and several to 10-times larger size at  $\theta_{\text{inc}} = 140^\circ$  (Fig. 2(e)).

Note that the sign of  $\delta(t_p)$  at small  $\Phi$  reverses at around  $\theta_{\text{inc}} \sim 45^\circ$  or  $\theta_{\text{inc}} - 90 \div 45^\circ$ , since  $\theta_{\text{inc}}$  almost coincides with the Cherenkov angle ( $\sim 45^\circ$ ) and then the relative magnitude of  $q_z$  of Cherenkov photons from  $\pi$  and  $K$  reverses (see Figs. 2(a), (e) and (f)). Thus, in the case of large  $L$ , as in Fig. 2(f),  $\delta(t_p)$  is cancelled with  $\delta(t_f)$ , which reduces the PID power compared with the small  $L$  case, as in Fig. 2(a).

### 2.3.2. $\pi/K$ separability

In the previous discussion, the expected resolution for the TOP measurement is given for the detection of a single Cherenkov photon. However, when we use the position-sensitive photon detector, we can use every Cherenkov photon to obtain PID information. In order to estimate the PID performance, we define the  $\pi/K$  separability ( $S_0$ ) as

$$S_0 = \sqrt{\left\{ \sum_i \left( \frac{\delta(t_p + t_f)^i}{(\sigma_T)^i} \right)^2 \right\}} \cdot \kappa. \quad (10)$$

In the calculation, individual  $\delta(t_p + t_f)^i$  and the total uncertainty  $(\sigma_T)^i$  arising from the above-mentioned items are obtained at every one-degree in  $\phi_C$  over a range of  $2\pi$ . The summation is taken over  $|\Phi| \leq 45^\circ$ , where the photons are totally reflected on the internal surface of the quartz bar.  $\kappa$  is the detectable portion of generated Cherenkov photons evaluated from Ref. [16].

In Fig. 3 the resultant  $S_0$  for  $\pi/K$  is presented as a function of the particle momentum ( $p$ ) for three different  $\theta_{\text{inc}}$ 's. For a normal incident particle, two cases are considered separately: (a) Cherenkov photons directly come to the photon detector (FW),

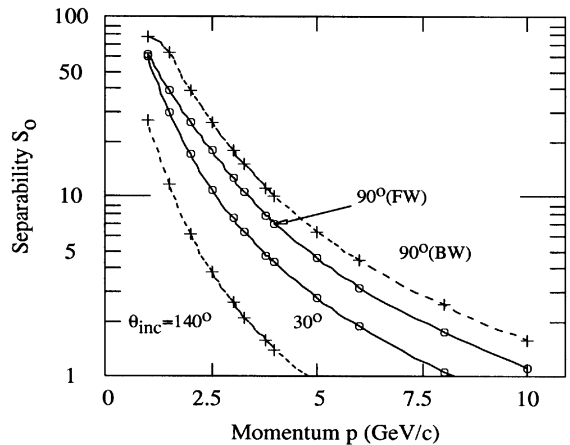


Fig. 3. Expected  $\pi/K$  separability ( $S_0$ ) vs. the momentum ( $p$ ) for different incidence angles ( $\theta_{\text{inc}}$ ). The solid and dotted curves correspond to the detection of forward (FW) and backward (BW)-going photons, respectively. The approximate numbers of detected photons are: 130 at  $\theta_{\text{inc}} = 30^\circ$ , 39 at  $\theta_{\text{inc}} = 90^\circ$  for both FW and BW photons, and 76 at  $\theta_{\text{inc}} = 140^\circ$  for  $p = 4 \text{ GeV}/c$  particles.

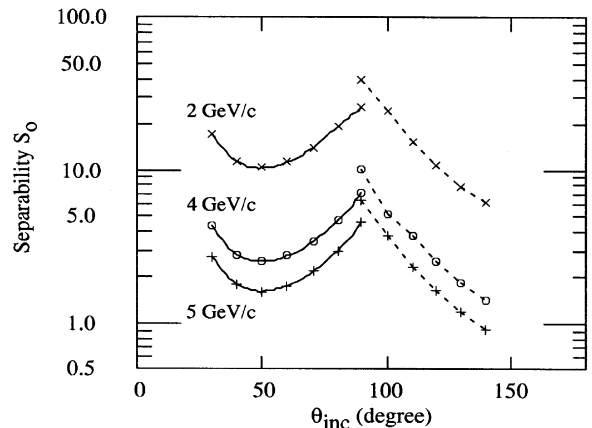


Fig. 4. Expected  $\pi/K$  separability ( $S_0$ ) as a function of  $\theta_{\text{inc}}$  for  $p = 2, 4$  and  $5 \text{ GeV}/c$ . In the regions of  $\theta_{\text{inc}} \leq 90^\circ$  and  $\geq 90^\circ$ , only the FW and BW-going photons are considered, respectively.

or (b) go to the backward end and then return to the detector (BW). A better separation is obtained for (b) because of the longer propagation distance of photons. The incident-angle dependence of  $S_0$  is shown in Fig. 4 for  $p = 2, 4$  and  $5 \text{ GeV}/c$  particles, where the FW and BW cases are indicated by the solid and dotted lines, respectively. The decrease

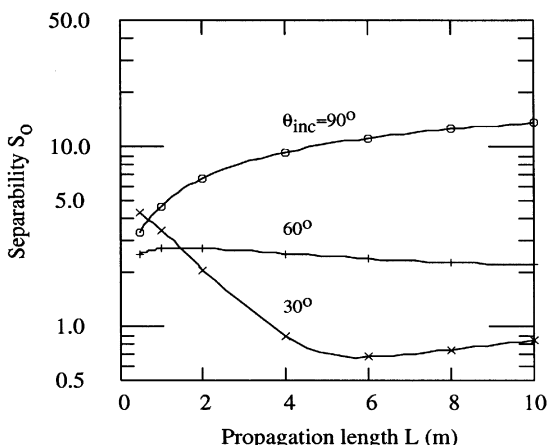


Fig. 5. Expected  $\pi/K$  separability ( $S_0$ ) as a function of the propagation length ( $L$ ) for  $\theta_{\text{inc}} = 30^\circ$ ,  $60^\circ$  and  $90^\circ$  and  $p = 4 \text{ GeV}/c$ .  $L$  is varied and only FW-photons are considered. The behaviour of  $S_0$  is discussed in the text.

in  $S_0$  around  $\theta_{\text{inc}} = 50^\circ$  is due to destructive correlation between  $\theta_{\text{inc}}$  and  $\theta_C$ , as mentioned above. The  $S_0$  variation on the propagation length ( $L$ ) is calculated by varying the quartz length for  $\theta_{\text{inc}} = 30^\circ$ ,  $60^\circ$  and  $90^\circ$  (FW), as shown in Fig. 5. At normal incidence,  $\delta(t_p + t_f)$  becomes large relative to the effects of (2) and (3)' as  $L$  increases, and, accordingly,  $S_0$  is improved. On the other hand, at around  $\theta_{\text{inc}} = 30^\circ$  the effect (1) becomes large with  $L$ , and  $S_0$  decreases, as can be seen in Figs. 2(a) and (f).

### 3. Simulation study

Based on the basic concepts considered in the preceding section, we carried out a simulation study on the realistic environment. Photons are generated following to the Cherenkov spectrum  $(dN(\lambda)/d\lambda)$  convoluted by the quantum efficiency  $\text{QE}(\lambda)$  of the phototube. The Cherenkov angle is determined by using the  $\lambda$ -dependent quartz refractivity ( $n(\lambda)$ ). The effect of the quartz thickness is naturally implemented in the simulation procedure. The effective TTS of the phototube is therefore set to be  $\sigma_{\text{TTS}} = 75 \text{ ps}$ , instead of the previous value of  $80 \text{ ps}$ , including the ambiguity of only the timing reference signal; this time resolution is considered

in smearing the calculated  $t_p + t_f$  values with a Gaussian of  $\sigma = \sigma_{\text{TTS}}$ . The phototube is assumed to detect only the earliest photon if multi-photons hit the same anode channel. The focussing resolution is also included by smearing the calculated  $\Phi$ -angle with a Gaussian of  $\sigma_\Phi = 0.5^\circ$  as well. Digitizations of the arrival time and  $\Phi$ -angle of photons are made in  $25 \text{ ps}$  and  $0.5^\circ$  bins, respectively. All other treatments are the same as in the previous calculation.

To display the various results for  $\pi$  and  $K$  tracks with the same momentum, we set parameters (as an example,  $p = 4 \text{ GeV}/c$  and  $\theta_{\text{inc}} = 90^\circ$ ) and require to detect only FW photons, unless the conditions are specified. Fig. 6(a) shows a typical  $\Phi$ -angle distribution of the number of detected photons for the  $\pi$  track. The number of produced photons is 137 in total, while the detected FW photons within  $|\Phi| = 45^\circ$  are 33. The photons distribute rather uniformly with an average of less than one per bin ( $\Delta\Phi = 0.5^\circ$ ). The  $t_p + t_f$  is shown in Fig. 6(b), where the circles and crosses are the detected photons radiated by the  $\pi$  and  $K$  track, respectively. They form two slightly asymmetric parabola-like distributions due to an inclined  $\phi_{\text{inc}}$ -angle by a deflection effect due to the magnetic field. It is  $4.3^\circ$  in this case. The dotted curves are the  $t_p + t_f$  calculated in the previous section by disregarding the  $\lambda$  dependences and generating photons with  $\theta_C = 1/n\beta$  ( $n = 1.47$ ). The upper two dotted curves in the figure correspond to the calculated  $t_p + t_f$  for the BW photons.

The deviations of  $t_p + t_f$  for an incident  $\pi$  and  $K$  from the calculated distribution assuming  $\pi$ ,  $\Delta(t_p + t_f)_{\pi/K}(\pi)$ , are presented in Fig. 6(c). In finding the deviation, two solutions exist at every  $\Phi$ -angle due to the above-mentioned deflection effect, so that we choose the smaller deviation as the correct one. The circles and crosses are for photons emitted by a  $\pi$  and a  $K$ , respectively. The former distributes around the null value, while the latter shifts to the positive side, as expected.

The solid and dotted histograms in Fig. 7 show the distribution of deviations,  $\Delta(t_p + t_f)_z(\beta)$ , for photons within  $|\Phi| \leq 45^\circ$ , where  $\alpha, \beta = \pi$  or  $K$ ; also,  $\alpha$  is the particle species of the track and  $\beta$  is the particle species assumed. The solid histogram presents the results under the correct assumption and

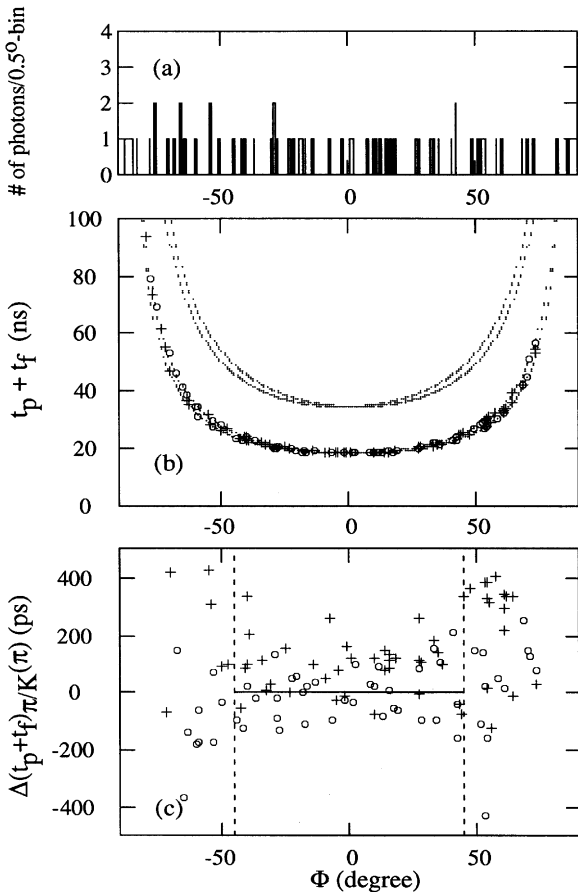


Fig. 6. Simulated results for a  $\pi$  and  $K$  track with  $p = 4 \text{ GeV}/c$  and  $\theta_{\text{inc}} = 90^\circ$ . Only FW-going photons are considered. (a) Detected number of photons vs.  $\Phi$  for a  $\pi$  track. In this case total number of photons produced is 137 and those detected within  $|\Phi| \leq 45^\circ$  is 33. (b)  $t_p + t_f$  as a function of  $\Phi$  for  $\pi$  ( $\circ$ ) and  $K$  ( $\times$ ). The dotted curves indicate the calculated  $t_p + t_f$ , of which details are described in the text. (c) Deviation of  $t_p + t_f$  from the calculated value assuming the pion,  $\Delta(t_p + t_f)_{\pi/K}(\pi)$ , for  $\pi$  ( $\circ$ ) and  $K$  ( $\times$ ).

the dotted histogram presents those under the incorrect assignment. Figs. 7(a) and (b) show typical deviations for an event, and Figs. 7(c) and (d) present the results for the accumulation of 100 tracks. We obtain the probability function ( $P(\pi/K)$ ) by fitting the results of the right assumption in Figs. 7(c) and (d) with Gaussian functions, as shown in the figures by the solid curves.

Based on this probability function, a log-likelihood ( $\ln \mathcal{L}$ ) under the assumption of  $\pi$  and  $K$ 's are

calculated for 400 tracks each for incoming  $\pi$  and  $K$ . Fig. 8(a) shows a scatter plot of the log-likelihoods thus obtained in the case of  $p = 4 \text{ GeV}/c$  and  $\theta_{\text{inc}} = 90^\circ$  for the FW photons; a clear separation between  $\pi$  and  $K$  can be seen. The separability ( $S$ ) is calculated by taking the difference in the log-likelihood ( $\Delta \ln \mathcal{L}$ ) between the two assumptions (see Fig. 8(b)) and using  $S = \sqrt{2 \Delta \ln \mathcal{L}}$ ;  $S = 5.7$  in this case. Thus, the calculated  $S$ 's for different  $p$ 's and  $\theta_{\text{inc}}$ 's are indicated in Fig. 9 for both FW and BW photons.

#### 4. Discussion and summary

We have shown that a high PID capability is attainable by using a  $(t_p, \Phi)$  measurement of the Cherenkov ring image. Although R&D is necessary, especially, on a high-quality position-sensitive phototube operable in a magnetic field and on an optimum focussing mirror, a good  $\pi/K$  separation is well expected at the Belle barrel detector.

Some remarks are given below:

- The development of a position-sensitive phototube is most important to realize the separability so far presented. It has twofold issues. One is to make it operable under a magnetic field and we have developed a fine-mesh-type multi-anode phototube for this purpose. The other is to remove or reduce the dead space dominated by the phototube package. The phototube (R5900U-00-L16) has a surface size of  $30 \text{ mm} \times 30 \text{ mm}$  in which the sensitive area is  $16 \text{ mm} \times 16 \text{ mm}$ , so that the effective area at our R&D counter becomes only about 40%. About half is in horizontal and 80% in the vertical. The required size of the phototube is  $20 \text{ mm} \times 100 \text{ mm}$  with a bin step of 1 mm for detecting photons with  $|\Phi| \leq 45^\circ$ .
- Adding the  $t_f$  information to the  $t_p$  information helps the PID, especially for low-momentum particles. However, for high-momentum particles its effect is not appreciable in our configuration. For instance, at  $4 \text{ GeV}/c$  tracks with  $\theta_{\text{inc}} = 90^\circ$ ,  $\delta(t_f)$  are 23 ps, which is only about 1/3 of  $\sigma_{\text{TTS}}$ . However, by setting a longer flight length ( $R$ ), a sizable improvement can be realized, as

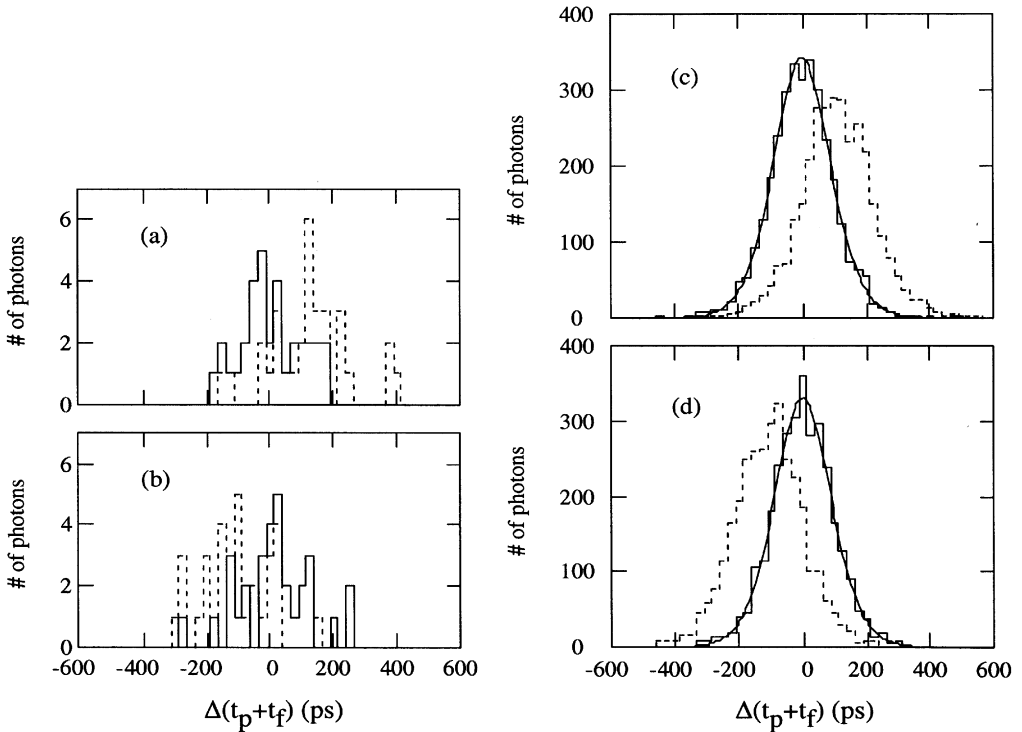


Fig. 7.  $\Delta(t_p + t_f)_z(\beta)$  distributions with  $|\Phi| \leq 45^\circ$  for FW-going photons for tracks of  $p = 4 \text{ GeV}/c$  and  $\theta_{\text{inc}} = 90^\circ$ . Solid (dotted) histogram presents the results under the correct (incorrect) assumption of  $\alpha = \beta$  ( $\alpha \neq \beta$ ). Tracks are assumed as  $\beta = \pi$  in (a) and (c), and as  $\beta = K$  in (b) and (d) to calculate the expected  $t_p + t_f$ . (a) and (b) are for the single tracks, while (c) and (d) are obtained by accumulating 100 tracks. Distributions with the right hypothesis are used as the probability function  $P(\pi/K)$ , whose functional form is obtained by fitting with Gaussian functions, as shown by the solid and dotted curves in (c) and (d), respectively.

listed in Table 1; in such cases the TOP detector acts as a kind of a high-resolution TOF counter by means of Cherenkov radiation, since the Cherenkov-angle difference does not produce sufficient  $\delta(t_p)$ .

- The  $\pi/K$  separability by the TOP measurement has an angular dependence, as can be seen in Fig. 9, while DIRC gives a more-or-less flat distribution with the incident angle. Especially, TOP shows a separability decrease at  $\theta_{\text{inc}} \sim 50^\circ$ , and it is in principle inevitable. On the other hand, TOP can give a larger  $S$  at normal incidence. Furthermore, in this case, TOP has the merit of doubling  $S$  by detecting both FW and BW going photons those of which have an arrival time difference of about 20 ns, so that they can be easily identified by using a multi-hit TDC with a high resolution.

- Because the present design of the focussing mirror has a horizontally extended structure, it is not suitable as a barrel detector, and therefore we need to find a partial optical structure for the compact system. Although the vertically configured mirror avoids this geometrical problem, the choice of the horizontal configuration is due to the fact that the  $t_p + t_f$  distribution for the vertical configuration has a larger differentiation to the angle  $\Theta$ , as shown in Fig. 10, so that the  $t_p + t_f$  measurement uncertainty becomes larger for an angle resolution of  $\Delta\Theta$  at the same accuracy as  $\Delta\Phi$ .

The simplest and practical solution for the above is to tilt the counter around the  $z$ -axis by an angle of, for instance,  $18.4^\circ$  ( $= \arctan(2 \text{ cm-thick}/6 \text{ cm-width})$ ) in our case, so that every mirror can avoid to interfere with each other.

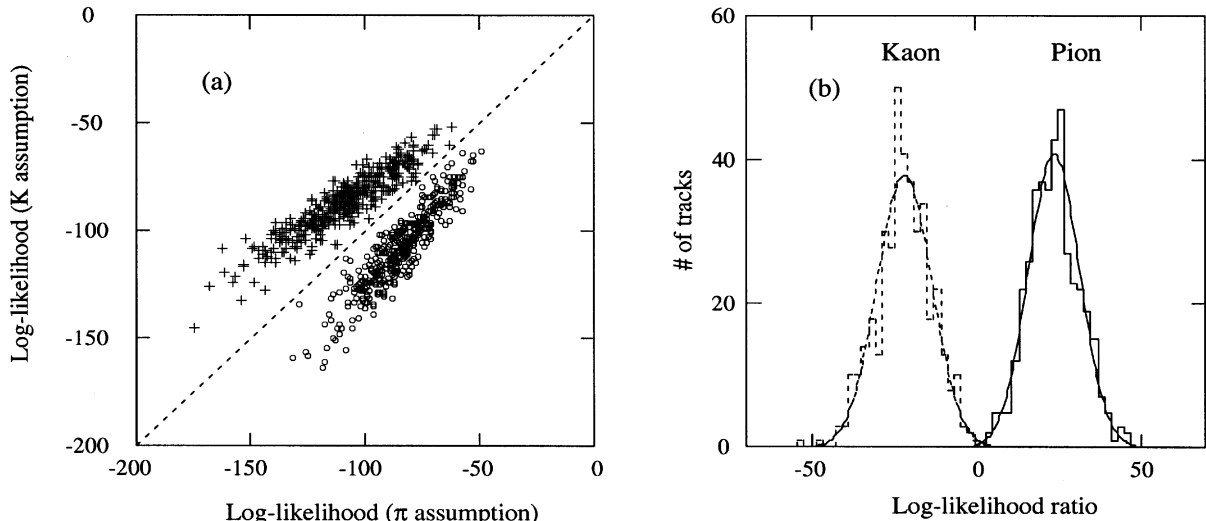


Fig. 8. Log-likelihood distributions of detected FW photons with  $|\Phi| \leq 45^\circ$  for  $\pi$  and  $K$  tracks with  $p = 4 \text{ GeV}/c$  and  $\theta_{\text{inc}} = 90^\circ$ . (a) Two-dimensional log-likelihood distributions for each  $400\pi$  ( $\circ$ ) and  $K$  ( $\times$ ) tracks are plotted for hypothesizing  $\pi$  (horizontal axis) and  $K$  (vertical axis). The dotted line indicates the equal  $\ln \mathcal{L}(\pi) = \ln \mathcal{L}(K)$  line. (b) Distributions of log-likelihood difference are shown for each  $400\pi$  (solid histogram) and  $K$  (dotted histogram) tracks. Curves are the Gaussian fitted to the data. The resulting  $S$  is 5.7 for this case.

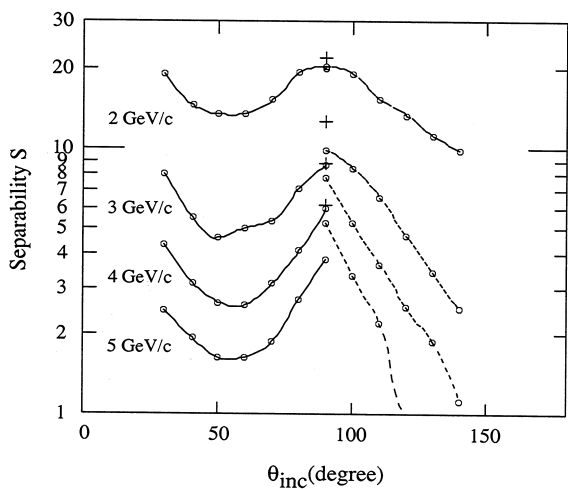


Fig. 9. Achievable separability ( $S$ ) vs.  $\theta_{\text{inc}}$  for  $p = 2, 3, 4$  and  $5 \text{ GeV}/c$   $\pi$  and  $K$  tracks. For the regions of  $\theta_{\text{inc}} \leq 90^\circ$  and  $\geq 90^\circ$ , the FW (solid curves) and BW (dotted curves)-going photons are detected, respectively. The  $S$  indicated by the plusses at  $\theta_{\text{inc}} = 90^\circ$  are by detecting both FW and BW photons:  $p = 2, 3, 4$  and  $5 \text{ GeV}/c$  from the upper to the lower point.

Table 1

Achievable separabilities ( $S$ ) with various flight-lengths ( $R$ ). The simulation results on our TOP detector, separately detecting FW and BW going photons, are listed for tracks with  $\theta_{\text{inc}} = 90^\circ$  under no magnetic field. The differences of  $\theta_C$  between  $\pi$  and  $K$  are 6.5 and 1.0 mrad for  $p = 4$  and  $10 \text{ GeV}/c$ , respectively, and those of the TOF are 231 and 37 ps at  $R = 10 \text{ m}$

Flight length $R$ (m)	Separability $S$			
	$p = 4 \text{ GeV}/c$		$p = 10 \text{ GeV}/c$	
	FW	BW	FW	BW
0		5.7	8.3	1.5
1		7.4	9.0	1.5
5		11.7	11.6	1.9
10		17.6	14.5	3.0

A TOP counter with a butterfly-shaped mirror, illustrated in Fig. 1, has a symmetrical geometry with respect to the  $z$ -axis. By dividing the butterfly mirror along the  $z$ -axis, a half butterfly-shaped counter can be constructable, although the bar

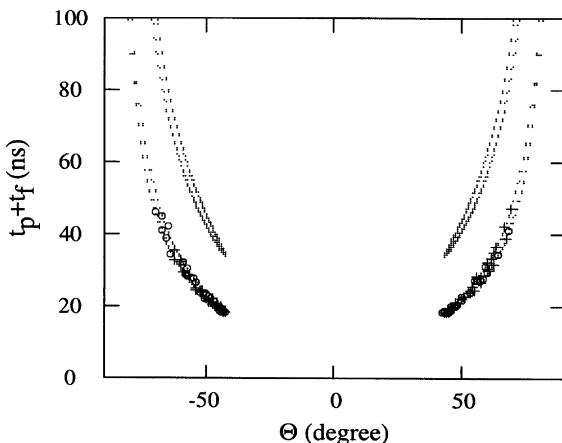


Fig. 10.  $t_p + t_f$  vs.  $\Theta$ .  $t_p + t_f$  of the same photons in Fig. 6(b) is plotted with  $\Theta$  instead of the  $\Phi$ -angle. The dotted curves indicate the calculated  $t_p + t_f$ , whose details are described in the text.

width also becomes half so as to have sufficient  $\Phi$ -angle resolution.

- For simplicity of the calculation, the probability function ( $P(\pi/K)$ ) is obtained in the previous section from the whole  $\Delta(t_p + t_f)$  distributions within  $|\Phi| = 45^\circ$ , while the spread of the distribution has the  $\Phi$ -dependence. Therefore, if we properly take account of this  $\Phi$ -dependence in the probability examination, better separability will be obtained. For instance, the rms of the distribution varies from 85 to 140 ps within the accepted  $\Phi$ -angle region in the case of 4 GeV/c normal incident tracks.
- We assumed the detection of only the earliest single photon at each photon tube anode in the previous section. It causes the loss of some photon fraction. For instance, it is about 30% of  $\approx 110$  detectable photons at  $\theta_{\text{inc}} = 30^\circ$ , while it is about 10% of  $\approx 56$  and  $\approx 30$  photons at  $\theta_{\text{inc}} = 60^\circ$  and  $90^\circ$ , respectively.

Although the above-mentioned issues concerning the phototube and the mirror structure remain, the proposed detector can be fully applicable as a PID device for experiments under a non-magnetic environment, mostly for fixed-target experiments. At fixed-target experiments, because incoming particles are incident nearly normal to the detector, the maximum separation power can be extracted.

The DIRC counter [2–4] verified that the Cherenkov image is well transported by internal total reflection, and the CCT counter [13–15] exhibited that a time measurement for such Cherenkov photons is feasible. While the TOP detector proposed here is based on a comprehensive compilation of the technical verification by those detectors, it can be used to exploit a new approach for measuring the  $t_p$  and  $\Phi$ -angle correlation by making use of the horizontal focussing mirror. As a result, it would not only provide high particle identification ability, but also a more compact and flexible detector compared with the DIRC and the gas Cherenkov imaging detector.

## Acknowledgements

We greatly thank Prof. Yoshitaka Kuno for informing us about the paper on the CCT counter. We also thank Prof. Katsumi Tanimura for his consultation on optics relating to our materials and devices. This work was supported by Grant-in-Aid for Scientific Research on Priority Areas (Physics of CP violation) from the Ministry of Education, Science, and Culture of Japan.

## References

- [1] J. Haba, Nucl. Instr. and Meth. A 368 (1995) 74.
- [2] T. Nozaki, Nucl. Phys. B 50 (Proc. Suppl.) (1996) 288.
- [3] B. Ratcliff, SLAC-Babar-Note-092 December 1992.
- [4] B. Ratcliff, SLAC-PUB-6047 January 1993.
- [5] P. Coyle et al., Nucl. Instr. and Meth. A 343 (1994) 292.
- [6] For instance, see D. Aston et al., IEEE Trans. Nucl. Sci. 42 (1995) 534.
- [7] H. Staengle et al., Nucl. Instr. and Meth. A 397 (1997) 261.
- [8] I. Adam et al., IEEE Trans. Nucl. Sci. 45 (1998) 450.
- [9] T. Kamae et al., KEK-Belle-49 April 1995.
- [10] T. Kamae et al., KEK-Belle-59 April 1995.
- [11] T. Kamae et al., Nucl. Instr. and Meth. A 382 (1996) 430.
- [12] T. Suito, Master Thesis, Nagoya University, 1998 (in Japanese).
- [13] K. Honscheid, M. Selen, M. Sivertz, Nucl. Instr. and Meth. A 343 (1994) 306.
- [14] D. Aronstein et al., Nucl. Instr. and Meth. A 371 (1996) 87.
- [15] H. Kichimi et al., Nucl. Instr. and Meth. A 371 (1996) 91.
- [16] Particle Data Group, Review of Particle Physics, European Phys. J. C 3 (1998) 155.